Acta Polytechnica CTU Proceedings **48**:27–33, 2024
https://doi.org/10.14311/APP.2024.48.0027

Published by the Czech Technical University in Prague

COMPARISON OF ELASTIC PROPERTIES OF PERIODIC AND APERIODIC POROUS STRUCTURES PRODUCED BY ADDITIVE METHODS

Radosław Grabiec[a,*], Jacek Tarasiuk[a,b], Sebasatian Wroński[a,b], Gianpaolo Pillon[c]

[a] *AGH - University of Cracow, al. Mickiewicza 30, 30-059 Cracow, Poland*

[b] *AGH - University of Cracow, Faculty of Physics and Applied Computer Science, Department of Condensed Matter Physics, Ul. Reymonta 19, 30-059, Cracow, Poland*

[c] *Université de Lorraine, Laboratoire d'étude LEM3 UMR CNRS 7239 7 rue Félix Savart, 57 070 Metz, France*

[*] corresponding author: rgrabiec@student.agh.edu.pl

Abstract. The aim of this work was to design, print, and examine elastic properties of porous structures with various parameters and beam distributions. These structures, generated using an algorithm, featured three types of lattices: octet, cubic, and Voronoi diagram-based, with different porosities (40 %, 60 %, 80 %) and beam sizes (0.45 mm, 0.66 mm). They were printed using Direct Light Processing and examined using X-ray computed microtomography. Compression tests were conducted to determine the Young's modulus. The results were compared with computer simulations performed using Abaqus. The tools used, such as 3D printing and X-ray computed microtomography, were described, and the results and conclusions of the tests were presented. As a result, comparable outcomes were obtained for structures with higher beam diameter, while significantly different results were observed for structures with lower beam diameter.

Keywords: Porous structures, elastic properties, FEM simulations, 3D printing, microtomography.

1. Introduction

Nowadays, structures characterized by porous structure are finding more and more interest and are often the object of research. The branches of industry, or science, that focus their attention mainly on such structures are: construction, chemistry, biology, medicine, and even automotive [1–3]. These structures can be of two types of mesh: periodic and aperiodic. The purpose of this research is to compare the elastic properties those structures obtained in the laboratory and the simulations. The main focus is on models based on Voronoi diagrams. Using a special algorithm, they were designed and then printed by Direct Light Processing (DLP) method. Once this was done, the porosity (80 %, 60 %, 40 %) of the print and the design were compared using a X-ray computed microtomography, and then the printed models were subjected to compression tests. Computer simulations were also performed on the same structures using Abaqus (Dassault Systèmes, France) software, and the results were compared. In the end, a value of Young's modulus was sought for which the experimental and simulation values give the same results. The work was carried out in collaboration with Gianpaolo Pillon, who performed strength tests and calculated Young's module for each of the designed and printed samples of the porous structures. The results are presented in the paper [4].

2. Materials and methods

2.1. Porous structure

In this work, aperiodic and periodic structures are compared. There are many types of meshes on which to base models of such structures. In this work, due to good knowledge of the parameters, meshes were chosen: octet and simple cubic for periodic structures (see Figure 1). Aperiodic structures were designed based on the Voronoi diagram (see Figure 1).

With this type of study, it is possible to see the dependence of elastic properties on: porosity, average thickness of beads and also the type of mesh.

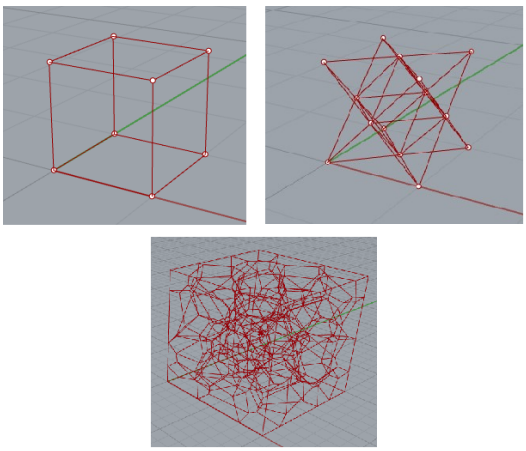

Figure 1. Examples of each unit cell: cubic and octet. Additionaly example of Voronoi diagram.

2.2. Structuring algorithm

In order to make the structures, improvements were needed to an algorithm previously made [5]. The algorithm was made using the Rhinoceros (Robert McNeel & Associates, USA) software and Grasshooper programming language [6]. The purpose of the algorithm is to create a given geometry, in this case a cube. After that, the cube is filled with the selected number and distribution of points. Depending on the selected distribution, a porous structure is formed on the basis of them. By operating the number of points and the diameter of the beams, it is possible to achieve the appropriate porosity of the model. Finally, it is possible to obtain three types of structures with a different distribution of beams: cubic, octet and based on the Voronoi diagram (see Figure 2). These types of meshes were chosen because cubic and octet decomposition often appear in the literature and are well known [7–11]. Voronoi structures, on the other hand, are less frequently addressed, and it was deemed worthwhile to compare well-studied structures with those that are not as well described.

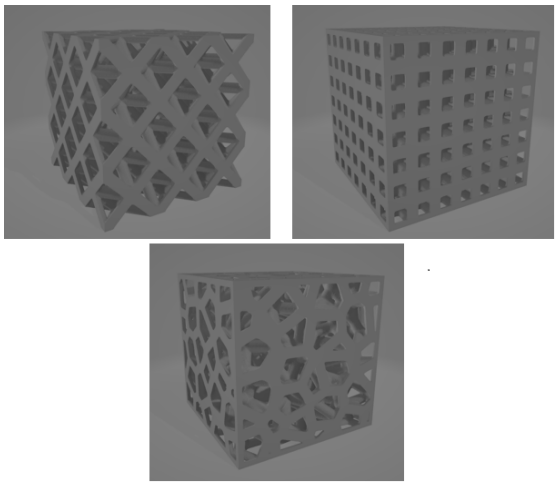

Figure 2. Examples of structures created by Grasshooper algorithm.

The porosity values chosen were 80 %, 60 %, 40 %. These values were a compromise between the capabilities of the 3D printer and the prospect of exploring more and less porous structures. The diameter of the beams was chosen so that for each type of bead distribution, the porosities and beam diameter would be similar. This is necessary for further comparison of models. The structures, designed in this way, were ready for printing.

2.3. Printing

Before printing, the structures need to be prepared in a specialized program Anycubic Photon slicer (see Figure 3), where printing parameters such as layer thickness, exposure time, number of initial layers are selected. In addition, the use of special supports is also needed. These are scaffolds with a lower density of material that holds the structure. The main parameters that were chosen were: Layer thickness 0.05 mm and exposure time of a single layer 8 seconds.

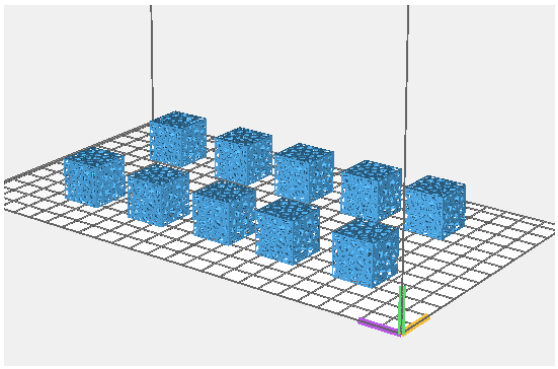

Figure 3. Anycubic photon slicer interface.

Each structure was printed five times, to obtain better statistics of the results during compression tests in the laboratory. The following are examples of the prints that were obtained (see Figure 4).

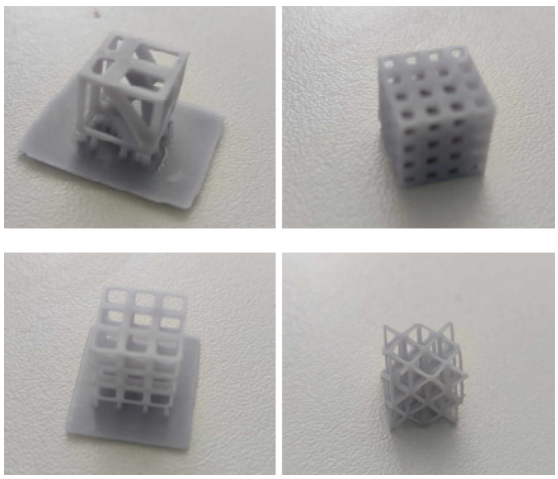

Figure 4. Example of printed structures.

2.4. MicroCT verified of printed structures

The microtomographic analysis of the printed structures was performed to compare the parameters of the printed and designed structures. The main attention was paid to the porosity and average thickness of the beads. A Nanotom S (Baker Hughes, USA) microtomograph was used for the study, while the VGStudio Max (Volume Graphics, Germany) program available in the laboratory was used to reconstruct the resulting scans. The X-ray tube parameters chosen were 70 kV accelerating voltage and 50 mA tube current. With these, it was possible to obtain images with a resolution of 15 μm, which was sufficient for beam diameters of around 0.5 mm. The resulting scans (see Figure 5) had to be edited in ImageJ Fiji [12]. Simple functions such as cropping, rotating, and the median filter, which averages pixels that are close together, were used.

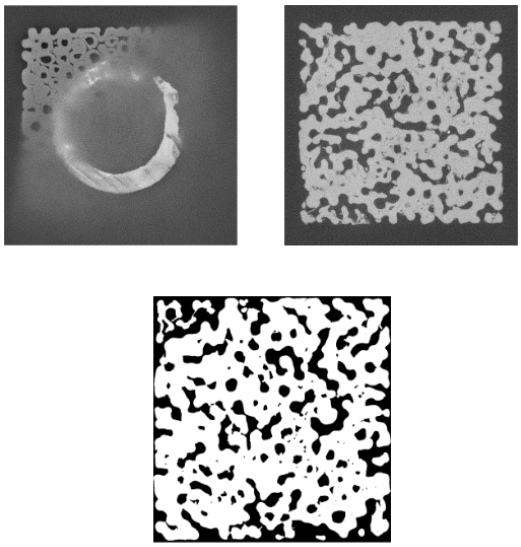

FIGURE 5. Example cross-section form Nanotom S microtomograph before and after editing. The image in the upper left corner, includes a cross-section in which a carbon tube is visible, on which the structure in the microtomograph is set. When editing, it is necessary to cut out the part of the cross-section on which it is located.

The sections were then binarized, resulting in black and white images. The white color represents the beams, while the black color is the air. Now, using the BoneJ plug-in [13], it is possible to calculate the ratio of pores to total volume and the average local thickness (see Figure 6) of the white parts of the images. This means that it is possible to get the porosity and the average thickness of the beams, as well as to depict the diameter distribution of the beams using histograms (see Figure 7). Table 1 summarizes the results of the design and printing.

It can be observed that the differences in porosity are small, at the level of a few percent. Some results were not taken into account during the study. This is because during printing, the resin remained in the center of the structure, subsequently distorting the results of porosity and beams thickness. In the case of the average thickness of the beads, the discrepancy is greater, at times exceeding 10 % and even 20 %. These discrepancies are particularly noticeable for the diameter of 0.45 mm beams. This result is a consequence of the printer's capabilities.

In the histograms (see Figure 7), it can be seen that the width of the range of the average thickness of the beams, when printed, is much greater. The thickness value heat map (see Figure 7), also shows that the discrepancy between the width of the beam and the node is greater in the case of printing. The distribution of the diameter of the beam itself is due to the presence of nodes, that is, places where the beams connect. These are those that have a different thickness than the beam itself. In printed structures, there are additional effects caused by the printing itself and its precision.

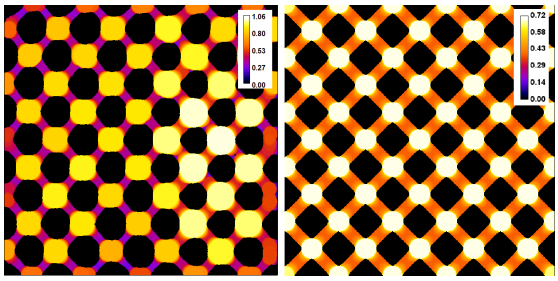

FIGURE 6. Comparison of the results of the *Thickness* function using a heat map. On the right is the map for the project, while on the left is the map for print.

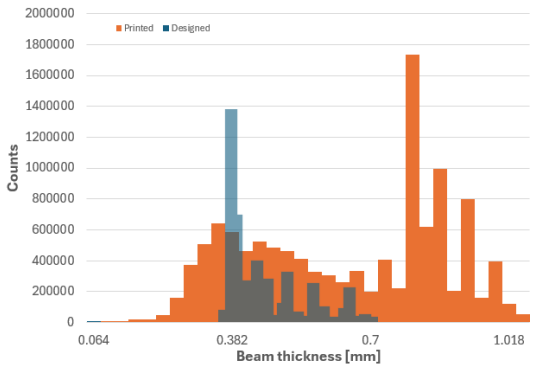

FIGURE 7. Histograms showing the distribution of beams thickness of printed and designed structure.

At times in the printed beam, a defect appeared, in the form of empty space. The function calculating the average diameter of the beams, treats such a space as two separate beams, which gives quite different values. In addition, during printing, because of the low values of the diameters, the resin is concentrated mainly in the beams, while the thicknesses of the beams themselves are underestimated. This can be seen in the histogram, as many peaks appear to the right of the main peak (see Figure 7). This may result in further problems during strength testing and simulation.

There were also mechanical problems during printing. In the center of the smaller diameter beams, cracks were noticed when reviewing the microtomography scans (see Figure 8). In addition, the edges of some structures were not printed (see Figure 8).

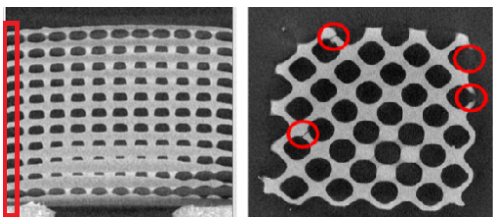

FIGURE 8. Examples of cracks, and side edge defects, caused by the printing process.

This problem can also be caused by sample storage. During drying, curing or handling them, due to the low diameter of the beams, cracking may have occurred.

$\mathbf{D_{D-beam}}$ [mm]	**Structure type**	**Design Porosity** [%]	**Printing Porosity** [%]	***Tb.th* Design** [mm]	***Tb.th* Printing** [mm]	**Porosity Relative difference** [%]	***Tb.th* Relative difference** [%]
0.66	Voronoi	80	83.00	0.69	0.69	3.8	0
	Voronoi	60	62.00	0.71	0.71	3.4	0
	Voronoi	40	38.00	0.73	0.75	5	2.7
	Cubic	80	84.00	0.63	0.70	5	11.1
	Cubic	60	63.00	0.71	0.79	5	11.2
	Cubic	40	—	0.76	—	—	—
	Octet	80	80.00	0.66	0.75	0	13.6
	Octet	60	59.00	0.72	0.79	1.66	9.7
	Octet	40	—	0.80	—	—	—
0.45	Voronoi	60	59.00	0.50	0.50	1.66	0
	Cubic	60	—	0.49	—	—	—
	Octet	60	60.00	0.51	0.65	15	27.5

Table 1. Table showing a comparison of the results of porosity and thickness measurements of print and design beams. $D_{\mathrm{D-beam}}$ describes the set diameter of the beams, while *Tb.th* describes the average thickness of the beams measured using the thickness function in ImageJ Fiji software.

2.5. Experimental results

Parallel to this research, experimental studies were also conducted on the printed structures described in this work. Because the structures were made from a light-curing resin, they had to be cured after printing. UV light was used for this. Each structure differs not only in the types of mesh, but also in the thickness and density of the beads. This means that the curing can be non-uniform. In order to determine the curing time, samples were cured for different amounts of time: 3 minutes, 6 minutes, 9 minutes, 15 minutes, 30 minutes, and then a compression test was performed on them and Young's modulus was calculated. By adjusting the curve, it was found that the curve becomes extinguished for a certain curing time. It was considered that 15 minutes would be a suitable time for each sample (a more detailed description can be found in the work of Gianpaolo Pillon). After that compression test was carried out, and then from the Stress–strain curve the Young's modulus was calculated by fitting a simple regression to the linear part of the graphs. This research was described in a paper by Gianpaolo Pillon. The most important results were the values of the calculated Young module (see Table 2). Looking at the standard deviation, it can be deduced that differences exist even at the level of the same structure. This shows the complexity of the repeatability of the whole process, as well as the storage of samples.

2.6. Designed structures FEA simulations

To determine the mechanical properties of designed structures using the Finite Element Method (FEM), it is necessary to know the Young's modulus value of the cured resin. Unfortunately, this value is not known, and it is uncertain whether the value obtained from tensile testing of a standard specimen dogbone shaped will be appropriate. Therefore, we decided to conduct a series of FEM simulations, continuously adjusting the assumed Young's modulus for the resin until the Young's modulus obtained from the simulations for the structure is close to the modulus obtained from measurements for the actual, printed structure.

Because the surface mesh generated by grasshopper consists of non-uniform triangles with different aspect ratio values, the remesh function in Meshlab was used. Figure 9 present model before and after remeshing. This function builds a renewal of the surface grid, which is much more homogeneous. The function has options for selecting the size of the triangles. However, it was remembered that the smaller the triangles, the more time-consuming the further research.

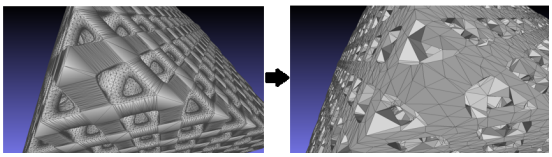

Figure 9. On the left Model generated by Rhinocerossoftware with grasshooper plugin and on the right model generated by Meshlab after remesh function.

A regular mesh has been achieved. The next step was to convert the surface grid to a volume grid. This is made possible by the Mesh 3D function in Gmsh software. The function parameters are set automatically by the environment. Default options were used, as no errors appeared in the software with these settings.

Using the Mesh 3D function, it is possible to simply convert the mesh. The theoretical models prepared in this way are ready to be imported into the Abaqus

Beam diameter [mm]	**Porosity** [%]	**Mesh**	**Seed**	**Young's modulus** [MPa]	**Std. Dev.** [MPa]
0.66	80	Voronoi	1	33.2	0.3
			2	46.2	1.4
			3	31.3	2.1
		Cubic	-	45.6	5.5
		Octet	-	45.5	0.9
	60	Voronoi	1	100.1	2.5
			2	122.8	5.5
			3	115	11
		Cubic	-	78.9	6.8
		Octet	-	112	13
	40	Voronoi	1	139	13
			2	146.5	5.3
			3	153.9	8.9
		Cubic	-	118	13
0.45	80	Voronoi	1	16.8	1.2
			2	30.7	2.7
			3	75	10.2
		Cubic		30.0	4.9
		Octet	-	25.7	2.6
	60	Voronoi	1	55.4	2.3
			2	67.5	3.4
		Cubic	-	73.5	7.4
		Octet	-	77	14
	40	Voronoi	1	156	12
			2	121	11

TABLE 2. Table compiling the results of compression tests in the laboratory. The determined Young's modulus is the average of five printed samples for each structure, from which the standard deviations were also determined.

program in which the simulations were performed.

At the beginning of each simulation, a random value of material's Young module was entered, which was then adjusted in the subsequent stages of the research to fit the behaviour of each structure. Two boundary conditions were imposed for this investigation. One of them was to block the lower wall of the cube that contained the structure. The purpose of such a condition was to make the structure unable to move and rotate in either direction. The second boundary condition, on the other hand, is the assignment of deformation to the upper wall. Due to such assumptions, the result of the simulation was the reaction forces achieved when obtaining a specific deformation. In the results section, it is possible to observe those reaction forces, deformations, and stresses at specific locations in the structures. We can see the acting stresses on the 3D model in the program, as well as export specific forces, such as those directed in a specific direction. This is illustrated in the form of arrows. The summed reaction force of the lower wall, inserted into the appropriate formula (see Equation 1), gave the result of the desired Young's modulus of each structure. This value was then compared with measured value. If the results differed, the Young's modulus of the material was changed and the analysis was repeated until the result matched this one from printed structure. Having the results of the structures from the laboratory, attempts were made to find such values of the Young's modulus of the material that the results for the structures themselves would be similar.

$$E = \frac{\sigma}{\epsilon} = \frac{F \cdot l_0}{A \cdot \Delta l} \tag{1}$$

F – reaction force [N],
l_0 – sample length [mm],
Δl – sample length's change [mm],
A – compressing surface [mm^2].

3. RESULTS

The above-described procedure was applied to all produced samples with various thicknesses of beams, different porosities, and different types of structure. As a result, it turned out that to ensure the Young's modulus values for each structure close to the values measured for real samples, we must assume different Young's modulus values for the hardened resin from which the samples were made (see Table 3 and Table 4). This means that the resin curing process occurred in different ways in different samples. Let us analyze these differences.

Structure type	**Porosity** [%]	**Lattice Young's Modulus from simulation** [MPa]	**Lattice Young's Modulus from printed models** [MPa]	**Material Young modulus** [MPa]
Voronoi	40	139	139	620
Voronoi	40	146	146	650
Voronoi	60	100	100	560
Voronoi	60	114	114	650
Voronoi	80	46	46	1000
Voronoi	80	31	31	650
Cubic	40	118	118	390
Cubic	60	79	79	550
Cubic	80	46	46	470
Octet	60	112	112	620
Octet	80	46	46	1150

Table 3. A table showing what Young's modulus of the material, had to be set so that the Young's modulus of the simulation structure coincides with that of the laboratory tests performed by Gianpaolo Pillon. Results for structures with 0.45 mm bead diameter.

Structure type	**Porosity** [%]	**Lattice Young's modulus from simulation** [MPa]	**Lattice Young's Modulus from printed models** [MPa]	**Material Young modulus** [MPa]
Voronoi	40	121	121	700
Voronoi	60	67	67	540
Voronoi	60	55	55	570
Voronoi	80	16	16	430
Voronoi	80	30	30	320
Cubic	60	74	74	350
Cubic	80	30	30	300
Octet	60	77	77	550
Octet	80	26	26	630

Table 4. A table showing what Young's modulus of the material, had to be set so that the Young's modulus of the simulation structure coincides with that of the laboratory tests performed by Gianpaolo Pillon. Results for structures with 0.45 mm bead diameter.

The results for structures with an average beam thickness of 0.66 mm (see Table 3) oscillate mostly around a certain average value in the range of 550–650 MPa. The problem arises particularly for two models: one based on the Voronoi diagram with 80 % porosity and the other on a cubic lattice with the same porosity. These discrepancies may be the result of the characteristics of the curing process. Because of the high porosity, UV light easily reaches every element of the structure. It is possible that for this type of structure, precisely because they are much better cured than the rest of the samples, the value of the determined Young's modulus may be significantly overestimated comparing to structures with more dense distribution of beams inside. Additionally, for the structure based on the Voronoi diagram, this issue may be due to the version in which it was designed, because the distribution of the beams in the structure determines its elastic properties. The results, although within a certain range, are not significantly similar. This may also be due to the diversity of the print itself. The standard deviations of the tests in the laboratory (see Table 2), show that for some structures the tests were more divergent than for others.

For structures with thinner beams (0.45 mm) (see Table 4), the situation is more complicated. Although there is not as much deviation for some structures as before, the values do not tend towards any narrow range. Their variability may be due to the reasons given in microtomography part, as well as a few additional effects (see Figures 6-9). During micro-CT scans for structures with a beam thickness of 0.45 mm, internal cracks occurred (see Figure 9). These cracks do not show regularity and are completely random. They are probably a result of the precision of print-

ing, which becomes significant with smaller strut sizes. Moreover, thin struts are more susceptible to mechanical damage that can occur, for example, during the washing or drying process of the structure. Under such sample preparation conditions, it is difficult to maintain homogeneity, which can result in differences, particularly for such thin beams.

4. Conclusions

Our assumption was that if it turned out that similar Young's modulus values were obtained for all structures made from the material from which the structures were printed, it would be possible in the future to model the properties of newly designed structures based on this universal value. Unfortunately, it turned out that depending on the type of structure, its porosity, and the size of the beams, the curing process occurred in different ways. Additionally, in some cases, the prints suffered from certain mechanical imperfections, which also affected their mechanical properties. All this means that in the future, it will not be possible to rely on a single Young's modulus value for the resin and model mechanical properties of designed structures based on it.

Summarizing this work, it was possible to obtain porous structures with the set parameters for three different types of meshes. In addition, the DLP 3D printing methodology was efficiently mastered, with minor problems (for example cracks (see Figure 9) most likely due to the resolution capabilities of the device. Microtomographic analysis showed that the porosity of the print was close to the design (see Table 1), while the average thickness of the beads deviated, also mainly due to the printing process itself. Results of the Young's Modulus of the material obtained using FEM for a diameter of 0.66 MPa, which must be set to enable the structure to exhibit similar elastic properties to those in the laboratory oscillate around the 500–600 MPa range with few exceptions (see Table 1). These results are acceptable. For structures with narrower beams, the results were much more complicated. Problems with these types of structures are mainly due to the printing and curing process. These results are good preparation for further research on porous structures, using other techniques to create a more reproducible measurement environment.

References

[1] N. A. Jaya, L. Yun-Ming, H. Cheng-Yong, et al. Correlation between pore structure, compressive strength and thermal conductivity of porous metakaolin geopolymer. *Construction and Building Materials* **247**:118641, 2020. https://doi.org/10.1016/j.conbuildmat.2020.118641

[2] P. Kowalczyk, M. Sprynskyy, A. P. Terzyk, et al. Porous structure of natural and modified clinoptilolites. *Journal of Colloid and Interface Science* **297**(1):77–85, 2006. https://doi.org/10.1016/j.jcis.2005.10.045

[3] Z. Liu, M. Fard, J. L. Davy. Prediction of the acoustic effect of an interior trim porous material inside a rigid-walled car air cavity model. *Applied Acoustics* **165**:107325, 2020. https://doi.org/10.1016/j.apacoust.2020.107325

[4] G. Pillon, R. Grabiec, J. Tarasiuk, et al. Tomograpic and mechanical study of 3D printed porous structure under compression load. *Acta Polytechnica CTU Proceedings* **48**:46–51, 2024. https://doi.org/10.14311/APP.2024.48.0046

[5] R. Grabiec, J. Tarasiuk, S. Wroński. Desing of the algorithm, print and analysis of porous structures with modifiable parameters. *Acta Polytechnica CTU Proceedings* **42**:27–31, 2023. https://doi.org/10.14311/app.2023.42.0027

[6] S. I. Rich, Z. Jiang, K. Fukuda, T. Someya. Well-rounded devices: the fabrication of electronics on curved surfaces – a review. *Materials Horizons* **8**(7):1926–1958, 2021. https://doi.org/10.1039/d1mh00143d

[7] N. Korshunova, G. Alaimo, S. B. Hosseini, et al. Image-based numerical characterization and experimental validation of tensile behavior of octet-truss lattice structures. *Additive Manufacturing* **41**:101949, 2021. https://doi.org/10.1016/j.addma.2021.101949

[8] K.-M. Park, Y.-S. Roh. Design optimization of additive manufactured edgeless simple cubic lattice structures under compression. *Materials* **16**(7):2870, 2023. https://doi.org/10.3390/ma16072870

[9] J. Feng, B. Liu, Z. Lin, J. Fu. Isotropic octet-truss lattice structure design and anisotropy control strategies for implant application. *Materials & Design* **203**:109595, 2021. https://doi.org/10.1016/j.matdes.2021.109595

[10] N. Novak, D. Kytyr, V. Rada, et al. Compression behaviour of TPMS-filled stainless steel tubes. *Materials Science and Engineering: A* **852**:143680, 2022. https://doi.org/10.1016/j.msea.2022.143680

[11] Y. Liu, J. Zhang, X. Gu, et al. Mechanical performance of a node reinforced body-centred cubic lattice structure manufactured via selective laser melting. *Scripta Materialia* **189**:95–100, 2020. https://doi.org/10.1016/j.scriptamat.2020.08.015

[12] J. Schindelin, I. Arganda-Carreras, E. Frise, et al. Fiji: an open-source platform for biological-image analysis. *Nature Methods* **9**(7):676–682, 2012. https://doi.org/10.1038/nmeth.2019

[13] M. Doube, M. M. Kłosowski, I. Arganda-Carreras, et al. BoneJ: Free and extensible bone image analysis in ImageJ. *Bone* **47**(6):1076–1079, 2010. https://doi.org/10.1016/j.bone.2010.08.023